

Banner appropriate to article type will appear here in typeset article

# Attenuation mechanism of wall-bounded turbulence by heavy finite-size particles

Yutaro Motoori<sup>†</sup> and Susumu Goto<sup>‡</sup>

Graduate School of Engineering Science, Osaka University, 1-3 Machikaneyama, Toyonaka, Osaka, 560-8531, Japan

(Received xx; revised xx; accepted xx)

To elucidate the attenuation mechanism of wall-bounded turbulence due to heavy small particles, we conduct direct numerical simulations (DNS) of turbulent channel flow laden with finite-size solid particles. When particles cannot follow the swirling motions of wall-attached vortices, vortex rings are shed around the particles. These shedding vortices lead to additional energy dissipation, reducing the turbulent energy production from the mean flow. This mechanism results in the attenuation of turbulent kinetic energy, which is more significant when the Stokes number of particles is larger or particle size is smaller. Moreover, we propose the method to quantitatively predict the degree of turbulence attenuation without using DNS data by estimating the additional energy dissipation rate in terms of particle properties.

## 1. Introduction

The addition of small particles can attenuate turbulence. This phenomenon has been demonstrated by many experiments since the last century. For example, [Gore & Crowe \(1989\)](#) compiled experimental results on turbulence modulation, demonstrating that when the particle diameter is about 0.1 times smaller than the integral length of turbulence, the particles can attenuate turbulence; otherwise, the larger particles enhance it. Although many authors ([Hosokawa & Tomiyama 2004](#); [Righetti & Romano 2004](#); [Tanaka & Eaton 2008](#); [Noguchi & Nezu 2009](#); [Yu \*et al.\* 2021](#)) proposed other parameters that characterize turbulence modulation, there is a consensus, supported by experiments ([Maeda \*et al.\* 1980](#); [Tsuji \*et al.\* 1984](#); [Kulick \*et al.\* 1994](#); [Rogers & Eaton 1991](#); [Fessler & Eaton 1999](#); [Kussin & Sommerfeld 2002](#); [Yang & Shy 2005](#)) and direct numerical simulations (DNS) ([Ferrante & Elghobashi 2003](#); [ten Cate \*et al.\* 2004](#); [Vreman 2007](#); [Zhao \*et al.\* 2010](#); [Abdelsamie & Lee 2012](#); [Zhao \*et al.\* 2013](#); [Li \*et al.\* 2016](#); [Liu \*et al.\* 2017](#); [Mortimer \*et al.\* 2019](#); [Oka & Goto 2022](#); [Peng \*et al.\* 2023](#)), that small heavy particles can lead to turbulence attenuation.

In addition to these studies, to accumulate a significant body of knowledge on the turbulence modulation due to particles, many researchers ([ten Cate \*et al.\* 2004](#); [Burton & Eaton 2005](#); [Lucci \*et al.\* 2010](#); [Yeo \*et al.\* 2010](#); [Bellani \*et al.\* 2012](#);

<sup>†</sup> Email address for correspondence: y.motoori.es@osaka-u.ac.jp

<sup>‡</sup> Email address for correspondence: s.goto.es@osaka-u.ac.jp

Wang *et al.* 2014; Schneiders *et al.* 2017; Uhlmann & Chouippe 2017; Oka & Goto 2022; Shen *et al.* 2022; Peng *et al.* 2023) conducted DNS of turbulence interacting with finite-size spherical particles in a periodic box. Among these studies, it is crucial to highlight the observation reported by ten Cate *et al.* (2004) that the energy dissipation rate produced by the relative motion between particles and fluid is a key quantity for significant attenuation of turbulent kinetic energy. In addition to their study, many authors (Squires & Eaton 1990; Elghobashi 1994; Kulick *et al.* 1994; Hwang & Eaton 2006; Mandø *et al.* 2009; Balachandar & Eaton 2010; Yeo *et al.* 2010; Wang *et al.* 2014) also emphasized the importance of the additional energy dissipation rate for turbulence attenuation. Recently, our group (Oka & Goto 2022) conducted DNS of periodic turbulence laden with finite-size particles and derived a formula to describe the turbulence attenuation rate. This formula is based on the physical picture of the turbulence attenuation that the additional energy dissipation due to particles bypasses the energy cascade. Balachandar *et al.* (2024) further developed this view to model interactions between particles and turbulence. Thus, the additional energy dissipation due to particles is crucial for turbulence attenuation. However, most of these results were obtained through numerical analyses of periodic turbulence without walls, although the pioneering studies on turbulence modulation by particles were made by experiments of air turbulence bounded by solid walls (Tsuji & Morikawa 1982; Tsuji *et al.* 1984; Kulick *et al.* 1994). Therefore, the next important issue is understanding the modulation mechanism of wall-bounded turbulence. This is the target of the present study.

Kulick *et al.* (1994) experimentally demonstrated that heavy copper particles attenuated turbulence intensity more effectively than glass particles. They concluded that as the relaxation time  $\tau_p$  of particles becomes longer than the time scale  $\tau_f$  of fluid motion, i.e., as the Stokes number  $St = \tau_p/\tau_f$  increases, the degree of turbulence attenuation becomes more significant. Note that the relaxation time is longer for heavier particles if they have the same diameter. Such  $St$ -dependence was also observed in DNS of turbulent channel flow with pointwise particles (Dritselis & Vlachos 2008, 2011; Lee *et al.* 2015; Wang & Richter 2019; Zhou *et al.* 2020). Although there are many DNS studies (Kajishima *et al.* 2001; Uhlmann 2008; Zeng *et al.* 2008; Shao *et al.* 2012; Fornari *et al.* 2016; Wang *et al.* 2016; Yu *et al.* 2017; Peng *et al.* 2019; Costa *et al.* 2020; Muramulla *et al.* 2020; Yu *et al.* 2021; Xia *et al.* 2021; Costa *et al.* 2021; Brandt & Coletti 2022) on the modulation of turbulent channel flow by finite-size particles, the physical picture of the modulation of wall-bounded turbulence remains unclear mainly because the phenomena depend on a large number of control parameters.

The purposes of the present study are (I) to understand the attenuation mechanism of wall-bounded turbulence by small heavy particles and (II) to predict the degree of turbulence attenuation in terms of particle properties. For these purposes, we conduct DNS of turbulent channel flow with finite-size spherical particles, systematically changing the particle diameter, mass density and turbulence Reynolds number. In particular, we focus on heavy particles as small as the buffer-layer coherent structures. To investigate the interaction between particles and turbulence, we assume that the gravitational effects are negligible.

In the following, we first describe the coupled DNS method for turbulent channel flow with particles (§ 2). Then, we examine the modulation of coherent vortices in real space (§ 3.1) and quantitatively investigate the modulation of energy

transfer mechanism (§§ 3.2–3.4). Then, based on this attenuation mechanism, we develop an argument to predict the degree of turbulence attenuation (§ 4).

## 2. Methods

### 2.1. Direct numerical simulations

We numerically simulate turbulence laden with finite-size particles between two parallel planes. The flow obeys the Navier–Stokes equation,

$$\frac{\partial \mathbf{u}}{\partial t} + (\mathbf{u} \cdot \nabla) \mathbf{u} = -\frac{1}{\rho_f} \nabla p - \frac{1}{\rho_f} \nabla P + \nu \nabla^2 \mathbf{u} + \mathbf{f}^{\bar{p}}, \quad (2.1)$$

and the continuity equation,

$$\nabla \cdot \mathbf{u} = 0, \quad (2.2)$$

where  $\mathbf{u}(\mathbf{x}, t)$  and  $p(\mathbf{x}, t)$  are the fluid velocity and the pressure at position  $\mathbf{x}$  and time  $t$ , respectively, and  $\rho_f$  and  $\nu$  denote the fluid mass density and kinematic viscosity, respectively. In (2.1),  $-\nabla P (= (-dP/dx, 0, 0))$  is a constant pressure gradient to drive flow, and  $\mathbf{f}^{\bar{p}}$  is the force per unit mass due to suspended particles. We evaluate this force using an immersed boundary method proposed by Breugem (2012). In this method, similarly to the original method by Uhlmann (2005), the force is evaluated to satisfy the non-slip boundary condition at the Lagrangian points distributed on the surface of each sphere.

We consider the motion of spherical solid particles with a mass density  $\rho_p$ , volume  $V_p$  and moment of inertia  $I_p$ . The equations of motion of a particle with velocity  $\mathbf{u}_p(t) = d\mathbf{x}_p/dt$  and angular velocity  $\boldsymbol{\omega}_p(t)$  are

$$\rho_p V_p \frac{d\mathbf{u}_p}{dt} = \oint_{\partial V_p} \boldsymbol{\tau}^{\bar{f}} \cdot \mathbf{n} \, dS + \mathbf{F}^{\bar{p}} \quad (2.3)$$

and

$$I_p \frac{d\boldsymbol{\omega}_p}{dt} = \oint_{\partial V_p} \mathbf{r} \times (\boldsymbol{\tau}^{\bar{f}} \cdot \mathbf{n}) \, dS + \mathbf{T}^{\bar{p}}. \quad (2.4)$$

Here,  $\boldsymbol{\tau}^{\bar{f}}$  is the stress tensor for a Newtonian fluid, and  $\mathbf{F}^{\bar{p}}$  and  $\mathbf{T}^{\bar{p}}$  are the force and torque acting on the particle due to collisions with other particles or solid walls, respectively. In (2.3) and (2.4),  $\mathbf{n}$  denotes the outward-pointing normal vector on the surface  $\partial V_p$  of the particle. By integrating (2.1) over the volume inside a sphere, we obtain the first term of the right-hand side of (2.3) as

$$\oint_{\partial V_p} \boldsymbol{\tau}^{\bar{f}} \cdot \mathbf{n} \, dS = -\rho_f \int_{V_p} \mathbf{f}^{\bar{p}} \, dV + \rho_f \frac{d}{dt} \int_{V_p} \mathbf{u} \, dV, \quad (2.5)$$

and that of (2.4) is given by  $\mathbf{r} \times (2.5)$ . We can therefore evaluate these terms from  $\mathbf{f}^{\bar{p}}$ . Then, we evaluate the second terms ( $\mathbf{F}^{\bar{p}}$  and  $\mathbf{T}^{\bar{p}}$ ) by using an elastic model (Glowinski *et al.* 2001) for the normal component of the contact force. We neglect the frictional force and collision torque.

To couple flow and particle motion, we alternately integrate their governing equations with the second-order Crank–Nicolson method for the viscous term of the fluid and explicit third-order low-storage three-step Runge–Kutta method for the others. Details of the numerical method are as described in Breugem (2012).

---

Table 1. Particle parameters.

$Re_\tau$	$D^+$	$D/h$	$D/\Delta$	$\rho_p/\rho_f$	$St_+$	$St_h$	$N_p$
512	16	0.031	8	2	28	0.056	8192
512	16	0.031	8	8	114	0.22	8192
512	16	0.031	8	32	455	0.89	8192
512	16	0.031	8	128	1820	3.6	8192
512	32	0.063	16	2	114	0.22	1024
512	32	0.063	16	8	455	0.89	1024
512	32	0.063	16	32	1820	3.6	1024
512	32	0.063	16	128	7282	14	1024
512	64	0.13	32	2	455	0.89	128
512	64	0.13	32	8	1820	3.6	128
512	64	0.13	32	32	7282	14	128
512	64	0.13	32	128	29127	57	128
360	16	0.044	8	2	28	0.078	2847
360	16	0.044	8	8	114	0.32	2847
360	16	0.044	8	32	455	1.3	2847
360	16	0.044	8	128	1820	5.1	2847
360	32	0.089	16	2	114	0.32	356
360	32	0.089	16	8	455	1.3	356
360	32	0.089	16	32	1820	5.1	356
360	32	0.089	16	128	7282	20	356
256	16	0.063	8	2	28	0.11	1024
256	16	0.063	8	8	114	0.44	1024
256	16	0.063	8	32	455	1.8	1024
256	16	0.063	8	128	1820	7.1	1024
256	32	0.13	16	2	114	0.44	128
256	32	0.13	16	8	455	1.8	128
256	32	0.13	16	32	1820	7.1	128
256	32	0.13	16	128	7282	28	128
180	16	0.089	8	2	28	0.16	356
180	16	0.089	8	8	114	0.63	356
180	16	0.089	8	32	455	2.5	356
180	16	0.089	8	128	1820	10	356

---

## 2.2. Parameters

We simulate turbulent channel flow at four values of the friction Reynolds number:  $Re_\tau = u_\tau h/\nu = 512, 360, 256$  and  $180$ , where  $u_\tau$  is the friction velocity and  $h$  is the channel half-width. The computational domain sizes are  $4h, 2h$  and  $2h$  in the streamwise  $x$ , wall-normal  $y$  and spanwise  $z$  directions, respectively. The grid width is  $\Delta^+ = 2$  for all directions. Here,  $\cdot^+$  denotes a quantity normalised by  $u_\tau$  and  $\nu$ . In the present study, for the normalisation (even in the case with the addition of particles), we use the value of  $u_\tau$  for the single-phase flow.

We add particles into turbulence in a statistically steady state. The particles are characterised by three parameters related to the diameter  $D$ , mass density  $\rho_p$

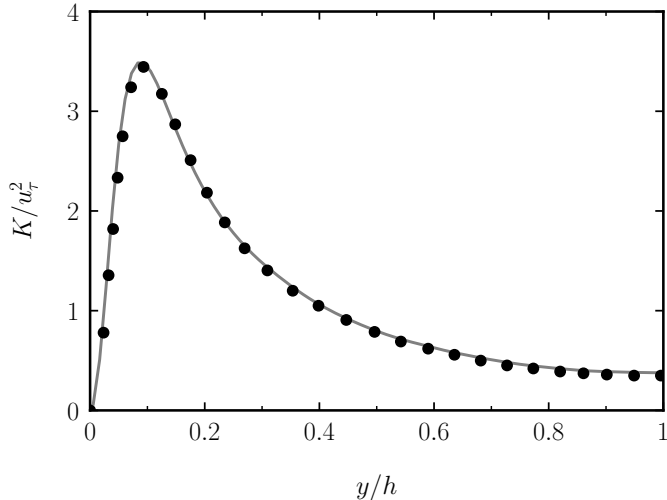


Figure 1. Wall-normal profile of the mean turbulent kinetic energy  $K(y)$ . The circles show the result by Yu *et al.* (2021). The parameters are  $D/h = 0.1$ ,  $\rho_p/\rho_f = 2$ ,  $\Lambda_0 = 0.0236$ ,  $u_{p,\infty}/U_b = 0.159$  and  $U_b(2h)/\nu = 5746$ . Data are extracted from figure 8(a) of their paper. The line shows the present DNS result with the same parameters.

and the number  $N_p$  of particles. Fixing the volume fraction  $\Lambda_0 (= N_p V_p / (16h^3))$  at 0.0082, we change the other two parameters:  $D$  and  $\rho_p$ . The particle diameters are  $D^+ = 16, 32$  and  $64$  for  $Re_\tau = 512$ ;  $D^+ = 16$  and  $32$  for  $Re_\tau = 360$  and  $256$ ; and  $D^+ = 16$  for  $Re_\tau = 180$ . We list in table 1 the parameters of particles. The particle diameters are comparable to or a few times larger than the diameter of tubular quasi-streamwise vortices in the buffer layer; but they are sufficiently smaller than the channel-half width (i.e.  $D/h \lesssim 0.1$ ). All particles are resolved to satisfy  $D/\Delta \geq 8$ , which is the same as in our previous studies (Oka & Goto 2022; Awai *et al.* 2024). For the mass density  $\rho_p$ , we set it to be larger than that  $\rho_f$  of the fluid:  $\rho_p/\rho_f = 2, 8, 32$  and  $128$ .

In the following, we show results on turbulence modulation using the relaxation time  $\tau_p$  of particles to the fluid motion instead of  $\rho_p/\rho_f$ . Here, we define the relaxation time as  $\tau_p = \rho_p D^2 / (18\rho_f \nu)$  by assuming the Stokes drag. We list in table 1 the values of  $St_+ = \tau_p / \tau^+$ , defined with the wall friction time  $\tau^+ (= \nu / u_\tau^2)$ , and  $St_h = \tau_p / \tau_h$ , defined with the largest eddy turnover time  $\tau_h = h / u_\tau$ . The examined particles have relaxation time  $\tau_p$  in a wide range between the swirling time scales of the smallest and largest vortices. Specifically, the shortest relaxation time ( $St_+ = 28$ ) is comparable to the time scale of coherent structures in the buffer layer (Soldati & Marchioli 2009). In other words, none of the simulated particles can thoroughly follow the swirl of streamwise vortices in the buffer layer. On the other hand,  $St_h (= St_+ Re_\tau)$  represents particles' ability to follow the largest vortices, that is, the wall-attached vortices in the outer layer. Particles with  $St_h \lesssim 1$  can follow the swirling motions of the outer-layer vortices, whereas those with  $St_h \gtrsim 1$  cannot follow them.

### 2.3. Validation

Before showing results in the next section, we validate our DNS by simulating particle-laden turbulence in the same system as investigated by Yu *et al.* (2021).

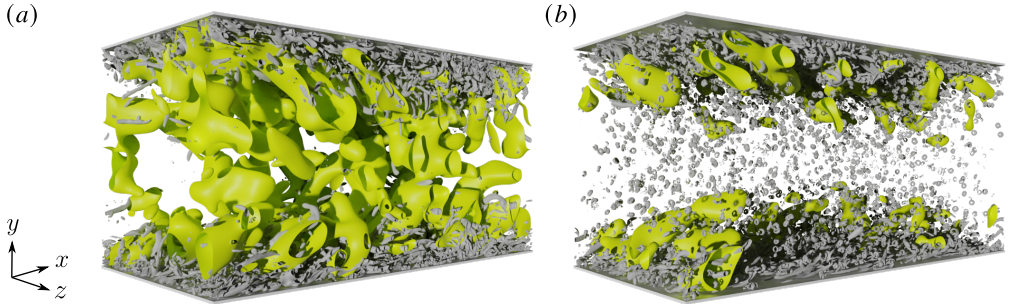


Figure 2. Visualisation of coherent vortices in turbulence at  $Re_\tau = 512$  laden with particles with the same diameter ( $D/h = 0.031$ , i.e.  $D^+ = 16$ ) but different values of the Stokes number: (a)  $St_h = 0.056$  and (b) 3.6. Grey vortices are identified by positive isosurfaces of the second invariant  $Q$  of the velocity gradient tensor. Yellow vortices are identified by the second invariant  $\widetilde{Q}^{(\ell)}$  of the velocity gradient tensor coarse-grained at  $\ell = 0.2h$ . We set the thresholds as  $Q^+ = 7.0 \times 10^{-3}$  and  $\widetilde{Q}^{(\ell)+} = 3.0 \times 10^{-5}$ .

For this, we impose a time-dependent pressure gradient to maintain a constant flow rate and apply the gravitational force to ensure that the ratio between the bulk mean velocity  $U_b$  and the terminal velocity  $u_{p,\infty}$  of particles is 0.159. Figure 1 shows the wall-normal profile of the mean turbulent kinetic energy,

$$K(y) = \frac{1}{2} \overline{\mathbf{u}'^2(\mathbf{x}, t)}, \quad (2.6)$$

in the statically steady state. Here,  $\overline{\cdot}$  denotes the average in the streamwise and spanwise directions and time, and  $\mathbf{u}'(\mathbf{x}, t) (= \mathbf{u}(\mathbf{x}, t) - \mathbf{U}(y))$  is the fluctuation fluid velocity, where  $\mathbf{U}(y) (= \overline{\mathbf{u}(\mathbf{x}, t)})$  is the mean velocity. We can confirm that our results are in good agreement with those of Yu *et al.* (2021). In the following analyses, we discuss the statistically steady state after adding the particles.

### 3. Attenuation mechanism

#### 3.1. Modulation of coherent vortices

First, let us examine the modulation of coherent vortices in turbulence. Figure 2 shows vortices in turbulence at  $Re_\tau = 512$  laden with the smallest ( $D/h = 0.031$ , i.e.  $D^+ = 16$ ) particles. The Stokes number differs between the panels: (a)  $St_h = 0.056$  and (b) 3.6. We show vortices at two different scales: the grey objects are the smallest vortices identified by positive isosurfaces of the second invariant  $Q$  of the velocity gradient tensor. To extract channel-half-width-scale vortices (i.e. wall-attached vortices in the outer layer), we apply the three-dimensional Gaussian filter (Motoori & Goto 2019) with filter width  $\ell = 0.2h$  to the fluctuation velocity. We then evaluate the second invariant  $\widetilde{Q}^{(\ell)}$  of the coarse-grained velocity gradient tensor and show its positive isosurfaces in yellow. It is evident in panel (a) that the yellow outer-layer vortices are developed even in the presence of particles with smaller  $St_h$  ( $= 0.056$ ); whereas, in panel (b), these vortices are almost entirely attenuated due to particles with larger  $St_h$  ( $= 3.6$ ).

It is also important to observe in figure 2(b) that vortex rings are shed from particles. Figures 3(a) and (b) are the magnifications of subdomains in figure 2(b) in the buffer and outer layers, respectively. Here, particles are depicted by white

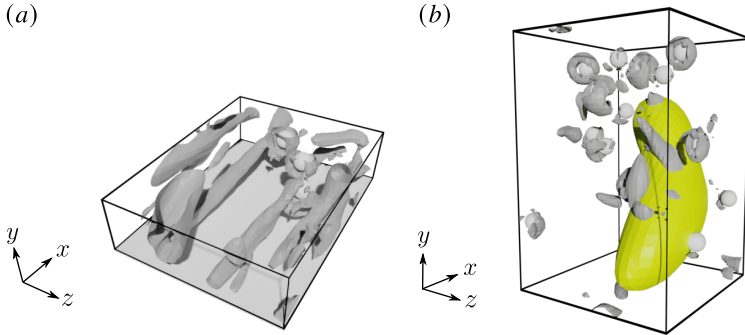


Figure 3. Magnification of subdomains in figure 2(b) for (a)  $0 \leq y^+ \leq 50$  and (b)  $0.3 \leq y/h \leq 0.75$  (i.e.  $154 \leq y^+ \leq 384$ ). Particles are depicted by white spheres.

spheres. There are many vortex rings around particles in the both layers. Since  $St_h$  of these particles is larger than 1, they can follow neither the outer-layer vortices (with the longest time scale in the turbulence) nor the buffer-layer vortices. The particles also cannot follow the mean flow because its time scale is comparable to the turnover time of the wall-attached vortices at each height. This explains the reason why these vortex rings are shed in the streamwise direction. In contrast, for  $St_h \ll 1$  (see figure 2a), there are no shedding vortices in the outer layer. These results therefore imply that the presence of shedding vortices results in the reduction of turbulent vortices. As will be discussed in detail in the following (see § 3.4), these shedding vortices are indeed important because they produce the additional energy dissipation, which is relevant to the turbulence attenuation.

### 3.2. Turbulent kinetic energy

To quantify the degree of turbulence modulation at each height, we evaluate the mean turbulent kinetic energy  $K(y)$  defined as (2.6). Figure 4 shows the wall-normal profiles of  $K(y)$  for turbulence at  $Re_\tau = 512$ . The blue dashed line indicates the value  $K_\times(y)$  for the single-phase flow, where the subscript  $\times$  denotes the value for the single-phase flow. First, let us look at panel (a), which shows the  $St_h$ -dependence for the smallest ( $D/h = 0.031$ ) particles. Lighter and thicker lines indicate results for larger  $St_h$ . We see in the panel that, irrespective of the height, turbulent kinetic energy is attenuated more significantly for larger  $St_h$ . This is consistent with the observation in figure 2 that particles with larger  $St_h$  more significantly attenuate outer-layer energetic vortices. More precisely, we can observe in figure 4 that as  $St_h$  increases,  $K$  is attenuated from the lower height. For example, particles with  $St_h = 0.056$ , that is  $St_+ = 28$  (the darkest and thinnest line), attenuate turbulence only for  $y/h \lesssim 0.1$  (i.e.  $y^+ \lesssim 50$ ). This is because the particle relaxation time is too long for them to follow the swirls of the buffer-layer vortices (whose time scale is in the order of  $10\tau_+$ ) but short enough to follow the larger wall-attached vortices such as the outer-layer vortices (because  $St_h \ll 1$ ). In contrast, particles with  $St_h = 3.6$  (the lightest line) attenuate the turbulent kinetic energy at any height. We observe similar behaviours for  $Re_\tau = 180$  (see the inset in figure 4a).

Figure 4(b) shows results for common  $St_h = 3.6$  but different values of  $D/h$  (darker and thinner lines indicate larger particles). Since  $St_h$  of these particles is larger than 1, they attenuate turbulence at all heights. It is however important

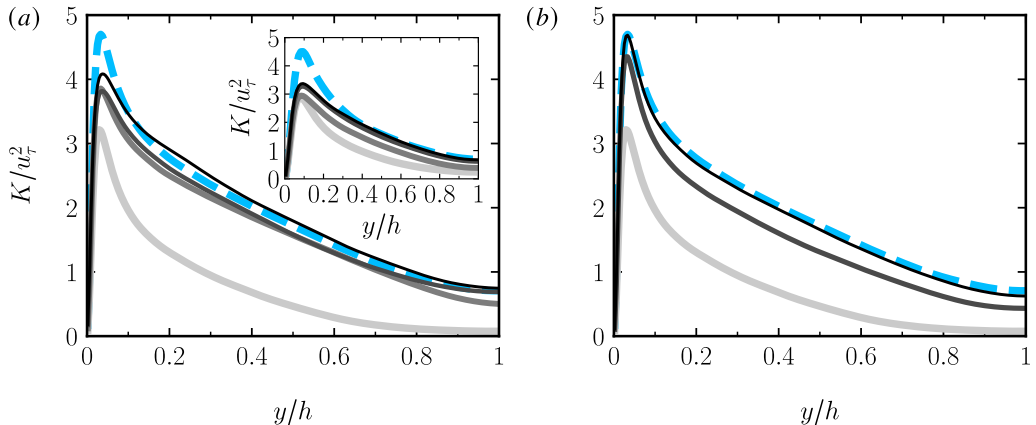


Figure 4. Wall-normal profiles of the mean turbulent kinetic energy  $K$  (2.6) at  $Re_\tau = 512$ . Panel (a) shows the Stokes-number-dependence [ $St_h = 0.056$  (black), 0.22 (dark grey), 0.89 (light grey) and 3.6 (very light grey)] for the common particle diameter  $D/h = 0.031$ , while (b) shows the particle-diameter-dependence [ $D/h = 0.031$  (black), 0.063 (grey) and 0.13 (light grey)] for the common Stokes number  $St_h = 3.6$ . The blue dashed line shows the result for the single-phase flow. The inset in (a) shows the results for  $Re_\tau = 180$  with  $St_h = 0.016$  (black), 0.63 (dark grey), 2.5 (light grey) and 10 (very light grey).

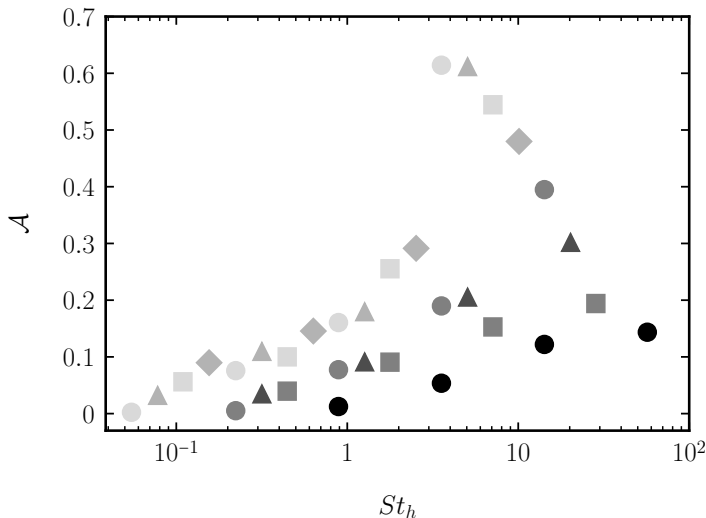


Figure 5. Average attenuation rate  $\mathcal{A}$  (3.1) of turbulent kinetic energy as a function of  $St_h$ . Different symbols show the results for  $Re_\tau = 512$  (circles), 360 (triangles), 256 (squares) and 180 (diamonds). The colour indicates  $D/h$  (lighter symbols indicate smaller particles).

to see in this panel that the attenuation rate depends on the particle size; more precisely, it is larger for smaller diameters.

Thus, when particles cannot follow the wall-attached vortices (and therefore the mean flow) at a given height  $y$ , the turbulent kinetic energy around  $y$  is attenuated. The degree of the turbulence attenuation is larger for larger Stokes numbers (figure 4a) and smaller diameters (figure 4b).

Next, we consider spatially averaged quantities. Figure 5 shows the average



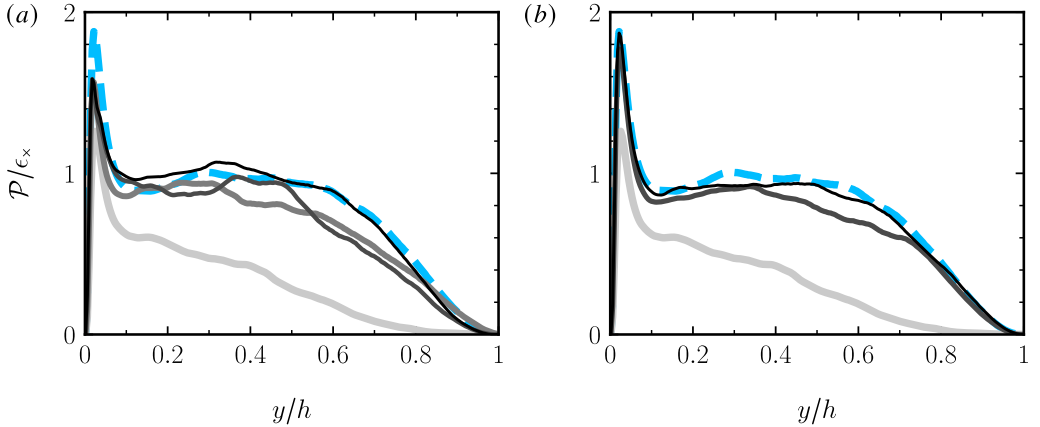


Figure 6. Wall-normal profiles of the mean turbulent energy production rate  $\mathcal{P}$  (3.2) at  $Re_\tau = 512$ . The values are normalised by the mean turbulent energy dissipation rate  $\epsilon_\times$  at each height in the single-phase flow. The lines in both panels indicate the same parameters as shown in figure 4.

attenuation rate,

$$\mathcal{A} = 1 - \frac{\langle K \rangle}{\langle K_\times \rangle}, \quad (3.1)$$

of turbulent kinetic energy as a function of  $St_h$ . Here,  $\langle \cdot \rangle$  denotes the spatial average. Lighter colours indicate smaller  $D/h$  and different symbols represent different values of  $Re_\tau$ . We can see that irrespective of  $Re_\tau$ , the average attenuation rate gets larger for larger  $St_h$  and smaller  $D/h$ . To explain these behaviours, in the following, we investigate how the energy transfers from the mean flow to small-scale vortices in the particle-laden turbulence.

### 3.3. Turbulent energy production by the mean flow

We evaluate the turbulent energy production rate

$$\mathcal{P}(y) = -\overline{u'v'} \frac{dU}{dy} \quad (3.2)$$

due to the mean flow. Figure 6 shows the wall-normal profiles of  $\mathcal{P}$  in turbulence at  $Re_\tau = 512$ . Here, we normalise  $\mathcal{P}(y)$  by the mean turbulent energy dissipation rate  $\epsilon_\times(y)$  ( $= 2\nu \overline{s'_{ij}{}^2}$ ) of the single-phase turbulence, where  $s'_{ij}$  is the strain-rate tensor for the fluctuation velocity. Particle parameters in figure 6 are the same as figure 4; namely, panel (a) shows results for the common  $D/h$  ( $= 0.031$ ) but different values of  $St_h$ , while (b) shows those for the common  $St_h$  ( $= 3.6$ ) but different values of  $D/h$ . Figure 6 shows that (i) when the Stokes number is larger or (ii) the particle size is smaller, the energy production rate tends to be more reduced.

Next, we show in figure 7(a) the spatial average  $\langle \mathcal{P} \rangle$  of the energy production rate normalised by the value  $\langle \mathcal{P}_\times \rangle$  in the single-phase flow as a function of  $St_h$ . The symbols are the same as in figure 5; namely, those in lighter colours indicate smaller  $D/h$ , and different shapes represent different values of  $Re_\tau$ . We see that the average production rate gets smaller for (i) larger  $St_h$  and (ii) smaller

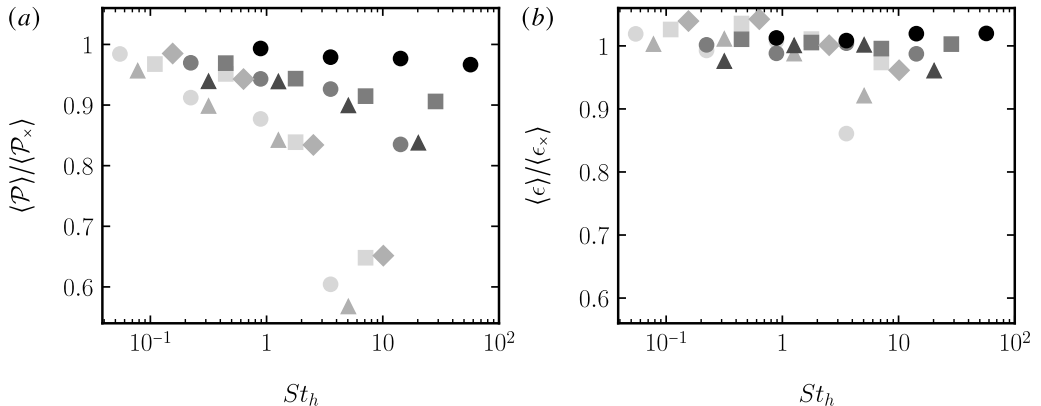


Figure 7. Spatial average of (a) turbulent energy production rate  $\langle \mathcal{P} \rangle$  by the mean flow and (b) turbulent energy dissipation rate  $\langle \epsilon \rangle$  as functions of  $St_h$ . The values are normalised by those in the single-phase flow. The symbols are the same as in figure 5.

$D/h$ . These behaviours are similar to those for turbulent kinetic energy shown in figures 4 and 5.

It is also important to observe that the turbulent energy dissipation rate  $\epsilon$  is not modulated by particles as much as  $\mathcal{P}$ . Figure 7(b) shows  $\langle \epsilon \rangle$  normalised by  $\langle \epsilon_x \rangle$  as a function of  $St_h$ . Note that  $\epsilon$  includes the two contributions from the energy dissipation through the energy cascade and from the wake behind added particles. We see that although  $\langle \epsilon \rangle$  is slightly reduced by the smallest and heaviest particles (indicated by the lightest circle), in most cases,  $\langle \epsilon \rangle / \langle \epsilon_x \rangle$  is close to unity. This result might be related to the fact that the mean velocity, and therefore the energy input rate  $-U \frac{dP}{dx}$  due to the pressure gradient are also not significantly altered in the present system (see Appendix A).

### 3.4. Additional energy dissipation due to particles

We have demonstrated in figures 6 and 7(a) that particles can reduce the energy production rate  $\mathcal{P}$ , which relates to the attenuation of turbulent kinetic energy. We have also shown in figures 2 and 3 that shedding vortices seem relevant to turbulence attenuation. In this subsection, we discuss how these shedding vortices contribute to the reduction of  $\mathcal{P}$ .

For the spatial average in the single-phase flow, the energy production rate by the mean flow is balanced by the energy dissipation rate, i.e.  $\langle \mathcal{P} \rangle \approx \langle \epsilon \rangle$ . However, particles can break this balance. More concretely, when particles cannot follow fluid motion, they create shedding vortices around themselves. Since these shedding vortices dissipate turbulent kinetic energy that would otherwise transfer from the mean flow to turbulent vortices, the energy production rate can be reduced. This implies that the reduction of the production rate is described as

$$\langle \mathcal{P} \rangle \approx \langle \epsilon \rangle - \langle \epsilon_p \rangle \quad (3.3)$$

in the particle-laden flow. Here,  $\langle \epsilon_p \rangle$  is the average energy dissipation rate per unit mass due to suspended particles. Since  $\langle \epsilon \rangle \approx \langle \epsilon_x \rangle$  holds in the present system as shown in figure 7(b), we can rewrite (3.3) as

$$1 - \frac{\langle \mathcal{P} \rangle}{\langle \mathcal{P}_x \rangle} \approx \frac{\langle \epsilon_p \rangle}{\langle \epsilon_x \rangle}. \quad (3.4)$$

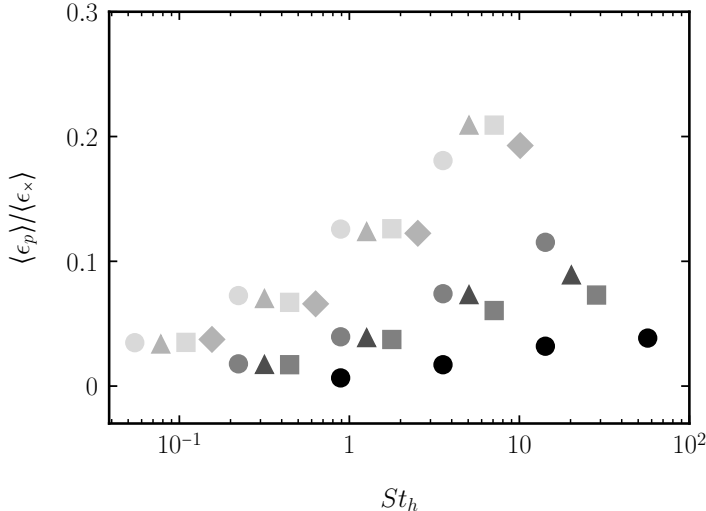


Figure 8. Spatial average  $\langle \epsilon_p \rangle$  of energy dissipation rate around particles defined with (3.5) as a function of  $St_h$ . The values are normalised by the spatial average  $\langle \epsilon_x \rangle$  of turbulent energy dissipation rate in the single-phase flow. The symbols are the same as in figure 5.

This equation means that the degree of the reduction of  $\langle \mathcal{P} \rangle$  is proportional to the energy dissipation rate  $\langle \epsilon_p \rangle$  due to particles.

To verify the above argument, we show in figure 8 the spatial average  $\langle \epsilon_p \rangle$  of the additional energy dissipation rate normalised by  $\langle \epsilon_x \rangle$ . Here, to estimate  $\langle \epsilon_p \rangle$ , we numerically compute the local average of the turbulent energy dissipation rate around all particles:

$$\langle \epsilon_p \rangle = \frac{1}{V_{\text{box}}} \left( \int_{\Omega_{\odot}} \epsilon(\mathbf{x}', t) dV' - V_{\odot} \bar{\epsilon} \right). \quad (3.5)$$

Here,  $\Omega_{\odot}$  is a spherical shell with diameter  $2.5D$  concentric with the particle,  $V_{\odot}$  is the volume of the spherical shell, and  $V_{\text{box}}$  is the volume of the computational box. The first term on the right-hand side of (3.5) captures the local average of the energy dissipation rate around particles. Since this quantity includes the dissipation rates due to not only the shedding vortices but also vortices generated by energy cascade or the mean shear, we subtract the latter contribution expressed by the second term. Figure 8 shows that  $\langle \epsilon_p \rangle$  gets larger for larger  $St_h$  or smaller  $D/h$ . We can explain these dependences by noting that the additional energy dissipation rate  $\epsilon_p$  around each particle is approximated by  $|\Delta u|^3/D$ , where  $\Delta u$  is the relative velocity. Hence, when (i) the Stokes number is larger, and therefore the relative velocity is larger or (ii) the diameter is smaller,  $\epsilon_p$  gets larger. Recall that figure 7(a) shows a similar tendency for the average reduction rate  $\langle \mathcal{P} \rangle$ . To verify this similarity, we show  $1 - \langle \mathcal{P} \rangle / \langle \mathcal{P}_x \rangle$  as a function of  $\langle \epsilon_p \rangle / \langle \epsilon_x \rangle$  in figure 9(a). The data approximately collapse on the red dotted line. This implies that we can describe the average reduction rate of the energy production due to the mean flow in terms of the additional energy dissipation rate  $\langle \epsilon_p \rangle$  by particles.

Moreover, the additional energy dissipation rate is also important in describing the average attenuation rate of turbulent kinetic energy. We show in figure 9(b) the average attenuation rate  $\mathcal{A}$ , defined as (3.1), of turbulent kinetic energy.

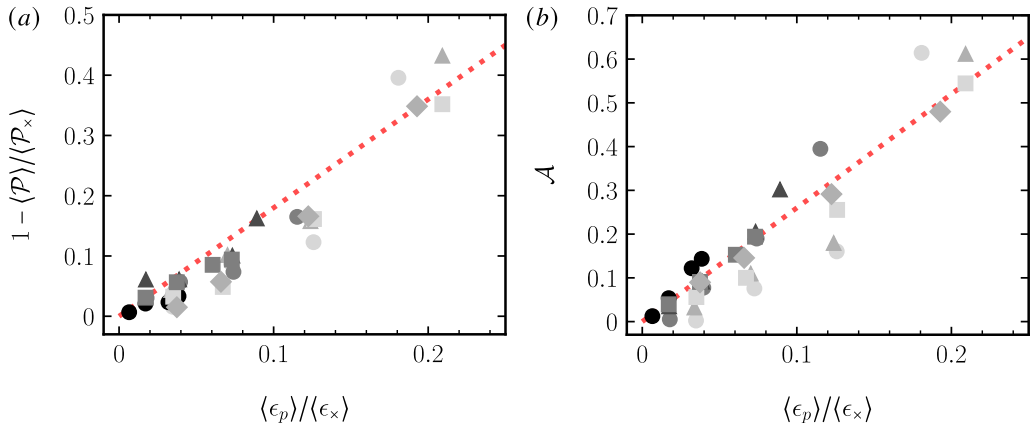


Figure 9. Average attenuation rate of (a) turbulent energy production rate by the mean flow and (b) turbulent kinetic energy as functions of  $\langle \epsilon_p \rangle / \langle \epsilon_x \rangle$ . The symbols are the same as in figure 5. The proportional coefficients of the dotted lines are (a) 1.8 and (b) 2.6, respectively.

Although the turbulence attenuation rate depends on  $St_h$ ,  $D/h$  and  $Re_\tau$  (see figure 5), when plotting  $\mathcal{A}$  as a function of  $\langle \epsilon_p \rangle / \langle \epsilon_x \rangle$ , the data approximately collapse on the red dotted line. We conclude therefore that the turbulence attenuation rate is approximately described in terms of the additional energy dissipation rate  $\langle \epsilon_p \rangle$  due to particles. Although some data points (e.g. the lightest circle and triangle) deviate from the red line, this deviation is caused by slight modulation of  $\langle \epsilon \rangle$  (see figure 7b).

We summarise the mechanism of attenuation of wall-bounded turbulence. When particles cannot follow the fluid motions and create the shedding vortices around them (figures 2 and 3), turbulent kinetic energy is attenuated (figure 4). This is because these shedding vortices produce the additional energy dissipation rate, preventing energy transfer from the mean flow to turbulent vortices (figures 6 and 7a). In contrast, particles do not significantly modulate the energy dissipation rate (figure 7b) and mean velocity (see figure 12a in Appendix A) for the examined parameters. This implies that they reduce the production rate  $\mathcal{P}$  of turbulent energy by reducing the Reynolds stress (figure 12b). Since the Reynolds stress is produced by wall-attached vortices (Lozano-Durán *et al.* 2012; Motoori & Goto 2021), turbulent kinetic energy  $K$ , which is related to these energetic vortices, is also attenuated. This is the reason why we can describe the average attenuation rates of  $\mathcal{P}$  and  $K$  in terms of the additional energy dissipation rate  $\langle \epsilon_p \rangle$  due to particles (figure 9).

#### 4. Prediction of turbulence attenuation rate

In this section, we propose a method to predict the degree of turbulence attenuation in terms of the given property of particles. To this end, we must predict the additional energy dissipation rate  $\langle \epsilon_p \rangle$ , which determines the turbulence attenuation rate, without the direct evaluation (3.5) as in the previous section.

#### 4.1. Estimation of particle energy dissipation

We first consider the magnitude of the force exerted on a particle by the fluid:

$$F^{\bar{f}} = \frac{1}{2} C_D \rho_f |\Delta u|^2 A, \quad (4.1)$$

where  $C_D$  is the drag coefficient,  $A$  ( $= \pi D^2/4$ ) is the cross-sectional area of the sphere, and  $\Delta u$  is the magnitude of the relative velocity. The particle subjected to this force leads to the energy dissipation at the rate of  $F^{\bar{f}} \Delta u$ . Therefore, the energy dissipation rate due to all the particles in the system can be expressed as

$$\langle \epsilon_p^\# \rangle = \frac{3}{4} \Lambda_0 C_D \frac{|\Delta u|^3}{D}. \quad (4.2)$$

Thus, to obtain  $\langle \epsilon_p^\# \rangle$ , we need to estimate the relative velocity  $\Delta u$ . We discuss the estimation of  $\Delta u$  in the next subsection.

Moreover, by estimating the average energy dissipation rate in the single-phase flow as  $\langle \epsilon_x^\# \rangle = u_L^3/h$  with  $u_L$  ( $\sim u_\tau$ ) being the characteristic velocity at the largest scale in the outer layer, we obtain

$$\frac{\langle \epsilon_p^\# \rangle}{\langle \epsilon_x^\# \rangle} = \frac{3}{4} \Lambda_0 C_D \frac{h}{D} \frac{|\Delta u|^3}{u_L^3}. \quad (4.3)$$

For the drag coefficient  $C_D$ , we use the experimental law (Schiller 1933):

$$C_D = \frac{24}{Re_D} (1 + 0.15 Re_D^{0.687}), \quad (4.4)$$

where  $Re_D$  ( $= |\Delta u|D/\nu$ ) is the particle Reynolds number. Thus, we can describe the additional energy dissipation rate (4.3) by using the particle parameters ( $\Lambda_0$  and  $D/h$ ) and the relative velocity  $\Delta u$ .

#### 4.2. Relative velocity

We show in figure 10 the relative velocity  $\langle |\Delta u| \rangle_o$  averaged in the outer layer ( $y/h \geq 0.3$ ) as a function of  $St_h$ . Note that since  $\Delta u$  strongly depends on height  $y$ , we focus on the outer layer where  $\Delta u$  weakly depends on  $y$  (see Appendix B). Here, we evaluate the relative velocity as  $\Delta u = \langle u \rangle_{\textcircled{p}} - u_p$ , where we define the surrounding fluid velocity  $\langle u \rangle_{\textcircled{p}}$  for each particle by the average fluid velocity on the surface of a sphere with diameter  $2D$  concentric with the particle (Kidanemariam *et al.* 2013; Uhlmann & Chouippe 2017). Symbols in lighter colours indicate smaller  $D/h$ , and different shapes represent different values of  $Re_\tau$ . We see in the figure that  $St_h$  determines the relative velocity irrespective of the other parameters. We also see that the functional forms of the relative velocity are well approximated by the dashed lines, which are defined as

$$\langle |\Delta u| \rangle_o = \begin{cases} \frac{(\tau_p/\tau_L)^{\frac{1}{2}}}{\sqrt{2}} u_L & (\tau_\eta \leq \tau_p \leq \tau_L), \\ \frac{\tau_p/\tau_L}{\sqrt{1 + (\tau_p/\tau_L)^2}} u_L & (\tau_p > \tau_L). \end{cases} \quad (4.5a)$$

$$(4.5b)$$

Here, (4.5a) holds when the particle relaxation time  $\tau_p$  is longer than the Kolmogorov time  $\tau_\eta$  and shorter than the integral time  $\tau_L$ , whereas (4.5b) holds for

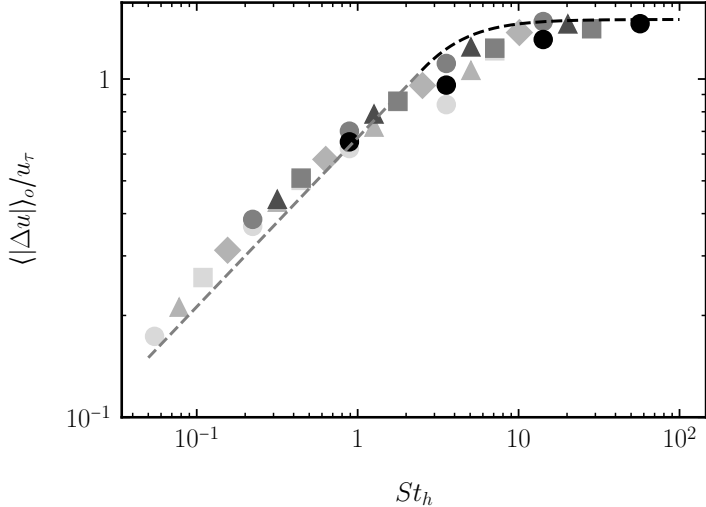


Figure 10. Relative velocity  $\langle \Delta u \rangle_o$  between particles and their surrounding fluid averaged in the outer layer. The symbols are the same as in figure 5. The grey and black dashed lines are evaluation by (4.5a) and (4.5b), respectively, with coefficients of  $u_L = 1.5u_\tau$  and  $\tau_L = 2.5\tau_h$ .

$\tau_p > \tau_L$ . We can derive (4.5) by assuming pointwise heavy particles based on the argument by Balachandar (2009) as follows. As considered in our previous studies (Oka & Goto 2021; Motoori *et al.* 2022), we first assume that the motion of particles with  $\tau_p$  is independent of fluid motions smaller than  $\ell$ , where  $\ell$  is the length scale such that the turnover time  $\tau^{(\ell)}$  ( $= \langle \epsilon_x \rangle^{-\frac{1}{3}} \ell^{\frac{2}{3}}$ ) of vortices with size  $\ell$  is approximately  $\tau_p$ , i.e.  $\ell = \langle \epsilon_x \rangle^{\frac{1}{2}} \tau_p^{\frac{3}{2}}$ . Then, considering a particle in the oscillating flow with the frequency  $\tau^{(\ell)}$  (Balachandar 2009), we obtain

$$\frac{\tilde{u}^{(\ell)} - u_p}{\tilde{u}^{(\ell)}} = \frac{\tau_p / \tau^{(\ell)}}{\sqrt{1 + (\tau_p / \tau^{(\ell)})^2}}. \quad (4.6)$$

Here,  $\tilde{u}^{(\ell)}$  is the fluid velocity coarse-grained at scale  $\ell$ . For  $\tau_\eta \leq \tau_p \leq \tau_L$ , when assuming that the relative velocity is determined by vortices whose turnover time is comparable to the particle relaxation time (i.e.  $\tau^{(\ell)} = \tau_p$ ), we can obtain (4.5a). In this derivation, we use  $\tilde{u}^{(\ell)} = \langle \epsilon_x \rangle^{\frac{1}{2}} \tau^{(\ell)\frac{1}{2}}$  and  $u_L = \langle \epsilon_x \rangle^{\frac{1}{2}} \tau_L^{\frac{1}{2}}$ . On the other hand, we can obtain (4.5b) for  $\tau_p > \tau_L$  by assuming that the relative velocity is determined by the largest-scale vortices (i.e.  $\tau^{(\ell)} = \tau_L$ ).

Figure 10 shows that (4.5) is in good agreement with our DNS data. Here, we choose the parameters  $u_L$  and  $\tau_L$  in (4.5) as in the order of  $u_\tau$  and  $\tau_h$ , respectively, so that the curves expressed by (4.5) fits our data. Incidentally, the relative velocity for  $\tau_p < \tau_\eta$  is determined by vortices at the Kolmogorov time scale (i.e.  $\tau^{(\ell)} = \tau_\eta$ ), although in the present study, we do not simulate particles with  $\tau_p < \tau_\eta$ .

Incidentally, it is not always possible to estimate the relative velocity using (4.5). This evaluation is valid when the particle diameter is smaller than the

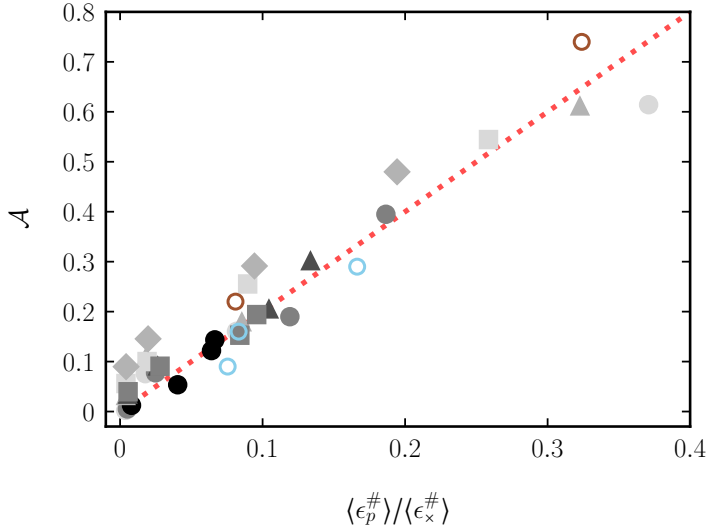


Figure 11. Average attenuation rate  $\mathcal{A}$  of turbulent kinetic energy as a function of  $\langle \epsilon_p^\# \rangle / \langle \epsilon_x^\# \rangle$ , which is estimated by (4.8) using only particle parameters. Particle parameters for the closed symbols are the same as in figure 5. The open circles show the turbulence attenuation rate at the channel centre measured in experiments by Kulick *et al.* (1994). The brown and light blue symbols indicate the results for coppers and glasses (with different volume fractions  $\Lambda_0$ ), respectively. The proportional coefficient of the dotted line is 2.

length scale  $\ell$  of vortices with the turnover time  $\tau^{(\ell)} \approx \tau_p$ , i.e.,

$$D \lesssim \ell \quad \Leftrightarrow \quad \frac{D}{h} \lesssim \begin{cases} (\tau_p/\tau_L)^{\frac{3}{2}} \approx St_h^{\frac{3}{2}} & (\tau_\eta \leq \tau_p \leq \tau_L), \\ 1 & (\tau_p > \tau_L). \end{cases} \quad (4.7a)$$

$$(4.7b)$$

The examined particles satisfy this condition.

#### 4.3. Prediction of turbulence attenuation rate

By substituting the relative velocity prediction (4.5) into (4.3), we can estimate the additional energy dissipation rate by

$$\frac{\langle \epsilon_p^\# \rangle}{\langle \epsilon_x^\# \rangle} = \begin{cases} \frac{3}{4} \Lambda_0 C_D \frac{h}{D} \frac{(\tau_p/\tau_L)^{\frac{3}{2}}}{2\sqrt{2}} & (\tau_\eta \leq \tau_p \leq \tau_L), \\ \frac{3}{4} \Lambda_0 C_D \frac{h}{D} \frac{(\tau_p/\tau_L)^3}{(1 + (\tau_p/\tau_L)^2)^{\frac{3}{2}}} & (\tau_p > \tau_L). \end{cases} \quad (4.8a)$$

$$(4.8b)$$

We plot in figure 11 the average attenuation rate  $\mathcal{A}$  as a function of  $\langle \epsilon_p^\# \rangle / \langle \epsilon_x^\# \rangle$ . We see that our DNS data collapse onto a single line, which is approximated by the red dotted line. In this figure, we also plot the experimental results (Kulick *et al.* 1994) for turbulent channel flow. The brown and light blue open symbols indicate the attenuation rates at the channel centre by copper and glass particles, respectively. Despite the different particle types and volume fractions, the experimental data align closely with our DNS results. Thus, we can use (4.8) to estimate the additional energy dissipation rate  $\langle \epsilon_p^\# \rangle / \langle \epsilon_x^\# \rangle$ , and by using this estimation, we can describe the turbulence attenuation rate.

Before concluding this article, we discuss the relevance to the study on periodic turbulence by [Oka & Goto \(2022\)](#). They derived the formula

$$1 - \left(1 - \frac{\mathcal{A}}{1 + \alpha}\right)^{\text{bit}} = \frac{\langle \epsilon_p \rangle}{\langle \epsilon_x \rangle} \quad (4.9)$$

for describing the turbulence attenuation rate, and then verified it using their DNS results of periodic turbulence. Here,  $\alpha$  is the ratio of the kinetic energy of the mean flow to turbulent energy for the single-phase flow. When deriving this formula, they first assumed that the additional energy dissipation rate bypasses the energy cascade. Then, they used [Taylor \(1935\)](#)'s dissipation law to relate average turbulent kinetic energy  $\langle K \rangle$  to its dissipation rate  $\langle \epsilon \rangle$ . We may use a similar relation between  $K$  and  $\epsilon$  ( $\approx \mathcal{P}$ ) in the log layer for wall-bounded turbulence at sufficiently high Reynolds numbers. However, since the present turbulence does not have a large scale separation to discuss the buffer, log and outer layers individually, we have argued the spatially averaged quantities. Nevertheless, our DNS results show that the turbulence attenuation rate increases monotonically with respect to  $\langle \epsilon_p \rangle / \langle \epsilon_x \rangle$  (see figure 9b). Moreover, we have demonstrated that  $\langle \epsilon_p \rangle / \langle \epsilon_x \rangle$  can be estimated based solely on particle parameters using (4.8). This estimation can be applicable to developed turbulence laden with small particles satisfying (4.7) in a dilute regime.

## 5. Conclusions

To investigate the attenuation of wall-bounded turbulence due to heavy small particles in a dilute regime, we have conducted DNS of turbulent channel flow laden with finite-size solid particles. Fixing the small volume fraction (0.82%) of particles, we change the particle diameter, particle relaxation time and turbulence Reynolds number (table 1). The conclusions of the present study are as follows.

When particles cannot follow the ambient fluid; namely, when the particle relaxation time is longer than the swirling time of the wall-attached vortices at the particles' existing height, vortex rings are shed from the particles (figures 2 and 3). The presence of such shedding vortices results in a significant turbulence attenuation (figures 4 and 5). This is because they produce the additional energy dissipation, which bypasses the energy production from the mean flow to turbulent vortices. This reduction of the energy production (see figure 6) is caused by the attenuation of turbulent vortices which are relevant to the production of the Reynolds stress (see figure 12b); consequently, turbulent kinetic energy is also attenuated. In contrast, the energy dissipation rate is not significantly modulated in the examined cases (figure 7b). Therefore, the energy production rate  $\mathcal{P}$  is reduced by the additional energy dissipation rate  $\epsilon_p$ . Our DNS results (figure 9a) show that this energy balance, described by (3.4), holds for the spatial averaging by numerically evaluating the additional energy dissipation rate  $\langle \epsilon_p \rangle$  (3.5). We also show that we can describe the average attenuation rate  $\mathcal{A}$  (3.1) of turbulent kinetic energy in terms of  $\langle \epsilon_p \rangle$  (figure 9b). This attenuation mechanism well explains the Stokes-number and particle-diameter dependence of  $\langle K \rangle$  (figure 5), since the energy dissipation rate  $\langle \epsilon_p \rangle$  due to particles becomes larger as (i) the Stokes number becomes larger or (ii) the particle size becomes smaller (figure 8).

To quantitatively predict the degree of turbulence attenuation, we estimate the relative velocity required for the estimation (4.3) of the additional energy



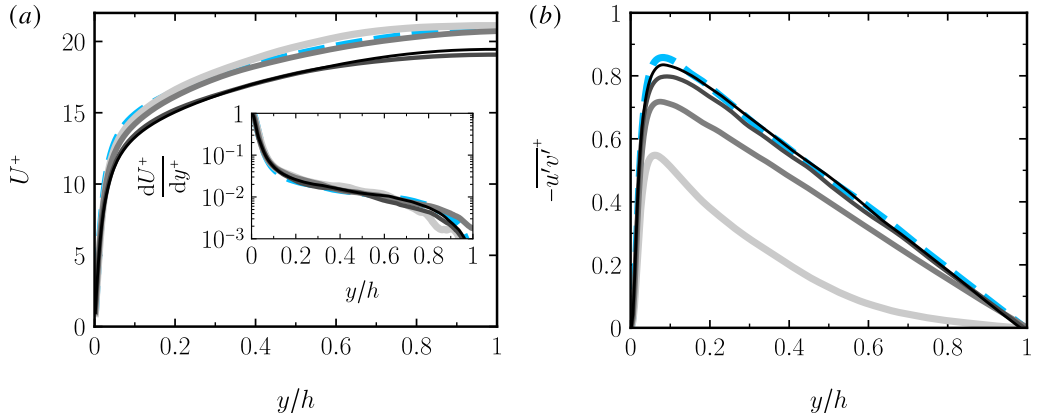


Figure 12. Wall-normal profiles of (a) the mean streamwise velocity  $U$  and (b) Reynolds stress  $-\overline{u'v'}$  at  $Re_\tau = 512$ . The lines indicate the same parameters as shown in figures 4(a) and 6(a). The inset in (a) shows the wall-normal profiles of the mean shear rate  $dU/dy$ .

dissipation rate  $\langle \epsilon_p^\# \rangle / \langle \epsilon_x^\# \rangle$ . Our DNS results (figure 10) demonstrate that the relative velocity averaged in the outer layer is determined by the functions (4.5) of  $St_h$ . These are derived based on the argument by Balachandar (2009) for heavy pointwise particles, allowing us to quantify  $\langle \epsilon_p^\# \rangle / \langle \epsilon_x^\# \rangle$  only from particle properties through (4.8). Moreover, our estimation of the average turbulence attenuation in terms of  $\langle \epsilon_p^\# \rangle / \langle \epsilon_x^\# \rangle$  well describes not only the present DNS data but also previous experimental results by Kulick *et al.* (1994) (figure 11).

## Acknowledgements

This study was partly supported by the JSPS Grants-in-Aid for Scientific Research 20H02068 and 23K13253. The DNS were conducted by using the computational resources of the supercomputers Fugaku through the HPCI System Research Projects (hp220232 and hp230288). The numerical analyses were conducted under the auspices of the NIFS Collaboration Research Program (NIFS22KISS010 and NIFS24KISC007). We would like to thank Professor Uhlmann for discussing the present study during our stay in Karlsruhe. We also thank Professor Balachandar for discussing the evaluation of the relative velocity.

## Declaration of interests

The authors report no conflict of interest.

## Appendix A. Mean velocity and Reynolds stress

We have shown in figure 6 the significant reduction of energy production rate  $\mathcal{P}$  from the mean flow. In this appendix, to show that this reduction is due to the attenuation of the Reynolds stress, we show in figure 12 the wall-normal profiles of (a) the mean streamwise velocity  $U$  and (b) Reynolds stress  $-\overline{u'v'}$  at  $Re_\tau = 512$ . Particle parameters are the same as in figure 6(a); namely, the results for the common  $D/h$  ( $= 0.031$ ) but different values of  $St_h$ . Looking at figure 12(a), we notice that the mean velocity and its gradients shown in the

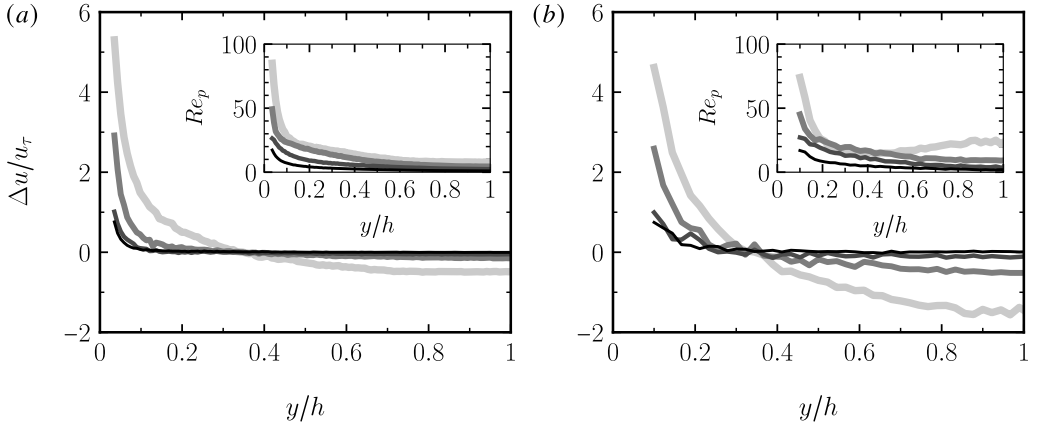


Figure 13. Wall-normal profiles of the mean relative velocity  $\Delta u(y)$  for  $D^+ = 16$  [i.e. (a)  $D/h = 0.031$  and (b)  $0.089$ ] in turbulence at (a)  $Re_\tau = 512$  and (b)  $180$ . The four lines in each panel show, from the thinner (and darker) to thicker (and lighter), (a)  $St_h = 0.056, 0.22, 0.89$  and  $3.6$ , and (b)  $St_h = 0.16, 0.63, 2.5$  and  $10$ . The insets show the particle Reynolds number  $Re_p(y)$ .

inset are not dramatically modulated from the single-phase flow (blue dashed line). In contrast, figure 12 (b) shows that the Reynolds stress is attenuated more significantly as  $St_h$  gets larger.

It is also worth mentioning that in the present system under the constant pressure gradient, since the mean flow profile is not much modulated, the energy input rate is almost constant. This might be the reason why the turbulent energy dissipation rate is also not modulated (see figure 7b).

## Appendix B. Wall-normal profile of the relative velocity

As mentioned in § 3.4, the relative velocity depends strongly on height. We can confirm this in figure 13, which shows the wall-normal profiles of the mean streamwise velocity difference  $\Delta u(y)$  for (a)  $Re_\tau = 512$  and (b)  $180$ . These results are for common  $D/h$  at each  $Re_\tau$  but for different  $St_h$ . The inset shows the particle Reynolds number  $Re_p(y) = |\Delta u(y)|D/\nu$ . We see that when  $St_h$  is larger,  $|\Delta u|$ , and therefore  $Re_p$ , are also larger. In the case of  $St_h \gtrsim 1$ , we also see that the sign of  $\Delta u$  changes around  $y/h \approx 0.3$  irrespective of  $Re_\tau$ . Since particles with  $St_h \gtrsim 1$  cannot follow the swirls of outer-layer vortices, they are slower than fluid in the outer layer. On the other hand, when the particles are swept out by the outer-layer vortices and move into the slower inner layer, the particles become faster than the fluid. Thus, the relative velocity behaves in a qualitatively different manner between the inner and outer layers. In § 4.2, we have defined the outer layer as  $y/h \geq 0.3$ , where  $\Delta u(y) > 0$ .

## REFERENCES

- ABDELSAMIE, A. H. & LEE, C. 2012 Decaying versus stationary turbulence in particle-laden isotropic turbulence: Turbulence modulation mechanism. *Phys. Fluids* **24**, 015106.
- AWAI, H., MOTOORI, Y. & GOTO, S. 2024 Attenuation of turbulence in a periodic cube by anisotropic solid particles. *submitted*.
- BALACHANDAR, S. 2009 A scaling analysis for point-particle approaches to turbulent multiphase flows. *Int. J. Multiph. Flow* **35**, 801–810.

- BALACHANDAR, S. & EATON, J. K. 2010 Turbulent dispersed multiphase flow. *Annu. Rev. Fluid Mech.* **42**, 111–133.
- BALACHANDAR, S., PENG, C. & WANG, L. P. 2024 Turbulence modulation by suspended finite-sized particles: Toward physics-based multiphase subgrid modeling. *Phys. Rev. Fluids* **9**, 044304.
- BELLANI, G., BYRON, M. L., COLLIGNON, A. G., MEYER, C. R. & VARIANO, E. A. 2012 Shape effects on turbulent modulation by large nearly neutrally buoyant particles. *J. Fluid Mech.* **712**, 41–60.
- BRANDT, L. & COLETTI, F. 2022 Particle-laden turbulence: progress and perspectives. *Annu. Rev. Fluid Mech.* **54**, 159–189.
- BREUGEM, W. P. 2012 A second-order accurate immersed boundary method for fully resolved simulations of particle-laden flows. *J. Comput. Phys.* **231**, 4469–4498.
- BURTON, T. M. & EATON, J. K. 2005 Fully resolved simulations of particle-turbulence interaction. *J. Fluid Mech.* **545**, 67–111.
- TEN CATE, A., DERKSEN, J. J., PORTELA, L. M. & VAN DEN AKKER, H. E. 2004 Fully resolved simulations of colliding monodisperse spheres in forced isotropic turbulence. *J. Fluid Mech.* **519**, 233–271.
- COSTA, P., BRANDT, L. & PICANO, F. 2020 Interface-resolved simulations of small inertial particles in turbulent channel flow. *J. Fluid Mech.* **883**, A54.
- COSTA, P., BRANDT, L. & PICANO, F. 2021 Near-wall turbulence modulation by small inertial particles. *J. Fluid Mech.* **922**, A9.
- DRITSELIS, C. D. & VLACHOS, N. S. 2008 Numerical study of educed coherent structures in the near-wall region of a particle-laden channel flow. *Phys. Fluids* **20**, 055103.
- DRITSELIS, C. D. & VLACHOS, N. S. 2011 Numerical investigation of momentum exchange between particles and coherent structures in low Re turbulent channel flow. *Phys. Fluids* **23**, 025103.
- ELGHOBASHI, S. 1994 On predicting particle-laden turbulent flows. *Appl. Sci. Res.* **52**, 309–329.
- FERRANTE, A. & ELGHOBASHI, S. 2003 On the physical mechanisms of two-way coupling in particle-laden isotropic turbulence. *Phys. Fluids* **15**, 315–329.
- FESSLER, J. R. & EATON, J. K. 1999 Turbulence modification by particles in a backward-facing step flow. *J. Fluid Mech.* **394**, 97–117.
- FORNARI, W., FORMENTI, A., PICANO, F. & BRANDT, L. 2016 The effect of particle density in turbulent channel flow laden with finite size particles in semi-dilute conditions. *Phys. Fluids* **28**, 033301.
- GLOWINSKI, R., PAN, T.-W., HESLA, T. I., JOSEPH, D. D. & PERIAUX, J. 2001 A fictitious domain approach to the direct numerical simulation of incompressible viscous flow past moving rigid bodies: application to particulate flow. *J. Comput. Phys.* **169**, 363–426.
- GORE, R. A. & CROWE, C. T. 1989 Effect of particle size on modulating turbulent intensity. *Int. J. Multiph. Flow* **15**, 279–285.
- HOSOKAWA, S. & TOMIYAMA, A. 2004 Turbulence modification in gas-liquid and solid-liquid dispersed two-phase pipe flows. *Int. J. Heat Fluids Flow* **25**, 489–498.
- HWANG, W. & EATON, J. K. 2006 Homogeneous and isotropic turbulence modulation by small heavy ( $St \sim 50$ ) particles. *J. Fluid Mech.* **564**, 361–393.
- KAJISHIMA, T., TAKIGUCHI, S., HAMASAKI, H. & MIYAKE, Y. 2001 Turbulence structure of particle-laden flow in a vertical plane channel due to vortex shedding. *JSME Intl J. Ser. B* **44**, 526–535.
- KIDANEMARIAM, A. G., CHAN-BRAUN, C., DOYCHEV, T. & UHLMANN, M. 2013 Direct numerical simulation of horizontal open channel flow with finite-size, heavy particles at low solid volume fraction. *New J. Phys.* **15**, 025031.
- KULICK, J. D., FESSLER, J. R. & EATON, J. K. 1994 Particle response and turbulence modification in fully developed channel flow. *J. Fluid Mech.* **277**, 109–134.
- KUSSIN, J. & SOMMERFELD, M. 2002 Experimental studies on particle behaviour and turbulence modification in horizontal channel flow with different wall roughness. *Exp. Fluids* **33**, 143–159.
- LEE, J., AHN, J. & SUNG, H. J. 2015 Comparison of large- and very-large-scale motions in turbulent pipe and channel flows. *Phys. Fluids* **27**, 025101.

- LI, D., LUO, K. & FAN, J. 2016 Modulation of turbulence by dispersed solid particles in a spatially developing flat-plate boundary layer. *J. Fluid Mech.* **802**, 359–394.
- LIU, C., TANG, S., SHEN, L. & DONG, Y. 2017 Characteristics of turbulence transport for momentum and heat in particle-laden turbulent vertical channel flows. *Acta Mechanica Sinica/Lixue Xuebao* **33**, 833–845.
- LOZANO-DURÁN, A., FLORES, O. & JIMÉNEZ, J. 2012 The three-dimensional structure of momentum transfer in turbulent channels. *J. Fluid Mech.* **694**, 100–130.
- LUCCI, F., FERRANTE, A. & ELGHOBASHI, S. 2010 Modulation of isotropic turbulence by particles of Taylor length-scale size. *J. Fluid Mech.* **650**, 5–55.
- MAEDA, M., HISHIDA, K. & FURUTANI, T. 1980 Velocity distributions of air-solids suspension in upward pipe flow: effect of particles on air velocity distribution. *JSME Ser. B (in Japanese)* **46**, 2313–2320.
- MANDØ, M., LIGHTSTONE, M. F., ROSENDAHL, L., YIN, C. & SØRENSEN, H. 2009 Turbulence modulation in dilute particle-laden flow. *Int. J. Heat Fluids Flow* **30**, 331–338.
- MORTIMER, L. F., NJOBUNWU, D. O. & FAIRWEATHER, M. 2019 Near-wall dynamics of inertial particles in dilute turbulent channel flows. *Phys. Fluids* **31**, 063302.
- MOTOORI, Y. & GOTO, S. 2019 Generation mechanism of a hierarchy of vortices in a turbulent boundary layer. *J. Fluid Mech.* **865**, 1085–1109.
- MOTOORI, Y. & GOTO, S. 2021 Hierarchy of coherent structures and real-space energy transfer in turbulent channel flow. *J. Fluid Mech.* **911**, A27.
- MOTOORI, Y., WONG, C. & GOTO, S. 2022 Role of the hierarchy of coherent structures in the transport of heavy small particles in turbulent channel flow. *J. Fluid Mech.* **942**, A3.
- MURAMULLA, P., TYAGI, A., GOSWAMI, P. S. & KUMARAN, V. 2020 Disruption of turbulence due to particle loading in a dilute gas-particle suspension. *J. Fluid Mech.* **889**, A28.
- NOGUCHI, K. & NEZU, I. 2009 Particle–turbulence interaction and local particle concentration in sediment-laden open-channel flows. *J. Hydro-Environ. Res.* **3**, 54–68.
- OKA, S. & GOTO, S. 2021 Generalized sweep-stick mechanism of inertial-particle clustering in turbulence. *Phys. Rev. Fluids* **6**, 044605.
- OKA, S. & GOTO, S. 2022 Attenuation of turbulence in a periodic cube by finite-size spherical solid particles. *J. Fluid Mech.* **949**, A45.
- PENG, C., AYALA, O. M. & WANG, L. P. 2019 Flow modulation by a few fixed spherical particles in a turbulent channel flow. *J. Fluid Mech.* **884**, A15.
- PENG, C., SUN, Q. & WANG, L. P. 2023 Parameterization of turbulence modulation by finite-size solid particles in forced homogeneous isotropic turbulence. *J. Fluid Mech.* **963**, A6.
- RIGHETTI, M. & ROMANO, G. P. 2004 Particle-fluid interactions in a plane near-wall turbulent flow. *J. Fluid Mech.* **505**, 93–121.
- ROGERS, C. B. & EATON, J. K. 1991 The effect of small particles on fluid turbulence in a flat-plate, turbulent boundary layer in air. *Phys. Fluids A* **3**, 928–937.
- SCHILLER, L. 1933 A drag coefficient correlation. *Zeit. Ver. Deutsch. Ing.* **77**, 318–320.
- SCHNEIDERS, L., MEINKE, M. & SCHRÖDER, W. 2017 Direct particle-fluid simulation of Kolmogorov-length-scale size particles in decaying isotropic turbulence. *J. Fluid Mech.* **819**, 188–227.
- SHAO, X., WU, T. & YU, Z. 2012 Fully resolved numerical simulation of particle-laden turbulent flow in a horizontal channel at a low Reynolds number. *J. Fluid Mech.* **693**, 319–344.
- SHEN, J., PENG, C., WU, J., CHONG, K. L., LU, Z. & WANG, L. P. 2022 Turbulence modulation by finite-size particles of different diameters and particle–fluid density ratios in homogeneous isotropic turbulence. *J. Turbulence* **23**, 433–453.
- SOLDATI, A. & MARCHIOLI, C. 2009 Physics and modelling of turbulent particle deposition and entrainment: Review of a systematic study. *Int. J. Multiph. Flow* **35**, 827–839.
- SQUIRES, K. D. & EATON, J. K. 1990 Particle response and turbulence modification in isotropic turbulence. *Phys. Fluids A* **2**, 1191–1203.
- TANAKA, T. & EATON, J. K. 2008 Classification of turbulence modification by dispersed spheres using a novel dimensionless number. *Phys. Rev. Lett.* **101**, 114502.
- TAYLOR, G. I. 1935 Statistical theory of turbulence iv-diffusion in a turbulent air stream. *Proc. R. Soc. Lond.* **151**, 465–478.
- TSUJI, Y. & MORIKAWA, Y. 1982 LDV measurements of an air-solid two-phase flow in a horizontal pipe. *J. Fluid Mech.* **120**, 385–409.

- TSUJI, Y., MORIKAWA, Y. & SHIOMI, H. 1984 LDV measurements of an air-solid two-phase flow in a vertical pipe. *J. Fluid Mech.* **139**, 417–434.
- UHLMANN, M. 2005 An immersed boundary method with direct forcing for the simulation of particulate flows. *J. Comput. Phys.* **209**, 448–476.
- UHLMANN, M. 2008 Interface-resolved direct numerical simulation of vertical particulate channel flow in the turbulent regime. *Phys. Fluids* **20**, 053305.
- UHLMANN, M. & CHOUÏPPE, A. 2017 Clustering and preferential concentration of finite-size particles in forced homogeneous-isotropic turbulence. *J. Fluid Mech.* **812**, 991–1023.
- VREMAN, A. W. 2007 Turbulence characteristics of particle-laden pipe flow. *J. Fluid Mech.* **584**, 235–279.
- WANG, G. & RICHTER, D. H. 2019 Two mechanisms of modulation of very-large-scale motions by inertial particles in open channel flow. *J. Fluid Mech.* **868**, 538–559.
- WANG, L. P., AYALA, O., GAO, H., ANDERSEN, C. & MATHEWS, K. L. 2014 Study of forced turbulence and its modulation by finite-size solid particles using the lattice Boltzmann approach. *Comput. Maths Applics.* **67**, 363–380.
- WANG, L. P., PENG, C., GUO, Z. & YU, Z. 2016 Flow modulation by finite-size neutrally buoyant particles in a turbulent channel flow. *Trans. ASME J. Fluids Engng* **138**, 041306.
- XIA, Y., LIN, Z., PAN, D. & YU, Z. 2021 Turbulence modulation by finite-size heavy particles in a downward turbulent channel flow. *Phys. Fluids* **33**, 063321.
- YANG, T. S. & SHY, S. S. 2005 Two-way interaction between solid particles and homogeneous air turbulence: Particle settling rate and turbulence modification measurements. *J. Fluid Mech.* **526**, 171–216.
- YEO, K., DONG, S., CLIMENT, E. & MAXEY, M. R. 2010 Modulation of homogeneous turbulence seeded with finite size bubbles or particles. *Int. J. Multiph. Flow* **36**, 221–233.
- YU, Z., LIN, Z., SHAO, X. & WANG, L. P. 2017 Effects of particle-fluid density ratio on the interactions between the turbulent channel flow and finite-size particles. *Phys. Rev. E* **96**.
- YU, Z., XIA, Y., GUO, Y. & LIN, J. 2021 Modulation of turbulence intensity by heavy finite-size particles in upward channel flow. *J. Fluid Mech.* **913**, A3.
- ZENG, L., BALACHANDAR, S., FISCHER, P. & NAJJAR, F. 2008 Interactions of a stationary finite-sized particle with wall turbulence. *J. Fluid Mech.* **594**, 271–305.
- ZHAO, L., ANDERSSON, H. I. & GILLISSEN, J. J. 2013 Interphasial energy transfer and particle dissipation in particle-laden wall turbulence. *J. Fluid Mech.* **715**, 32–59.
- ZHAO, L. H., ANDERSSON, H. I. & GILLISSEN, J. J. 2010 Turbulence modulation and drag reduction by spherical particles. *Phys. Fluids* **22**, 081702.
- ZHOU, T., ZHAO, L., HUANG, W. & XU, C. 2020 Non-monotonic effect of mass loading on turbulence modulations in particle-laden channel flow. *Phys. Fluids* **32**, 043304.